Journal of *Marine Science and Engineering*

MDPI

Article

Investigation on Wake Characteristics of Two Tidal Stream Turbines in Tandem Using a Mobile Submerged PIV System

Sejin Jung [1,†], Heebum Lee [2,†], In Sung Jang [1], Seong Min Moon [1], Heungchan Kim [1], Chang Hyeon Seo [1], Jihoon Kim [1,*] and Jin Hwan Ko [3,*]

[1] Korea Institute of Ocean Science and Technology, Busan 49111, Republic of Korea; sjjung@kiost.ac.kr (S.J.); isjang@kiost.ac.kr (I.S.J.); smmoon@kiost.ac.kr (S.M.M.); hckim@kiost.ac.kr (H.K.); chseo@kiost.ac.kr (C.H.S.)
[2] Central Research Institute, Korea Hydro & Nuclear Power Co., Ltd., Daejeon 34101, Republic of Korea; heebum.lee@khnp.co.kr
[3] Department of Mechanical System Engineering, Jeju National University, Jeju 63243, Republic of Korea
* Correspondence: jihoonkim@kiost.ac.kr (J.K.); jko@jejunu.ac.kr (J.H.K.)
† These authors contributed equally to this work.

Abstract

Understanding wake interactions between multiple tidal stream turbines is essential for optimizing the performance and layout of tidal energy farms. This study investigates the hydrodynamic behavior of two horizontal-axis tidal turbines arranged in tandem under simplified inflow conditions, where the incoming flow was dominated by the streamwise velocity component without imposed external disturbances. Wake measurements were conducted in a large circulating water tunnel using a mobile, submerged particle image velocimetry (PIV) system capable of long-range, high-resolution measurements. Performance tests showed that the downstream turbine experienced a decrease of approximately 9% in maximum power coefficient compared to the upstream turbine due to reduced inflow velocity and increased turbulence generated by the upstream wake. Phase-averaged PIV results revealed the detailed evolution of velocity deficit, turbulence intensity, turbulent kinetic energy, and tip vortex structures. The tip vortices shed from the upstream turbine persisted over a long downstream distance, remaining coherent up to 10D and merging with those generated by the downstream turbine. These merged vortex structures produced elevated turbulence and complex flow patterns that significantly influenced the downstream turbine's operating conditions. The results provide experimentally validated insight into turbine-to-turbine wake interactions and highlight the need for high-fidelity wake data to support array optimization and numerical model development for tidal stream turbine array.

Keywords: tidal energy; horizontal-axis tidal stream turbine; wake interaction; tandem turbine configuration; particle image velocimetry (PIV)

Academic Editor: Decheng Wan

Received: 8 December 2025
Revised: 29 December 2025
Accepted: 6 January 2026
Published: 8 January 2026

1. Introduction

Tidal energy has emerged as one of the most promising renewable energy resources due to its predictability, high energy density, and minimal environmental and visual impact. As global interest in tidal energy expands, research has increasingly shifted from isolated single-turbine studies to multi-turbine farm configurations, where wake interactions become a dominant factor influencing overall farm performance [1,2]. Wake effects are particularly important because downstream turbines are strongly affected by the velocity deficit, turbulence levels, and vortex structures generated by upstream devices,

leading to reduced efficiency and increased unsteady loading [3,4]. One of the major challenges in designing tidal stream turbine arrays is understanding and predicting wake behavior—its development, dissipation, and interaction with nearby turbines.

Kang et al. [3] conducted experimental measurements using Acoustic Doppler Velocimetry (ADV) to investigate wake interactions between two tandem horizontal-axis tidal turbines with a diameter of 0.16 m. A comparison between the 5D and 7D spacing cases showed that the turbulence characteristics in the downstream turbine wake were largely insensitive to turbine spacing. The study suggested that the incoming turbulence intensity is the dominant factor governing wake characteristics within tidal turbine arrays.

McNaughton et al. [4] experimentally investigated the effects of inter-turbine spacing on the performance and loading of a co-planar tidal turbine fence. Towing-tank experiments were conducted using two model turbines with a diameter of 1.2 m. The results showed that reducing lateral spacing increased local blockage, leading to a consistent improvement in the fence-averaged power coefficient. The performance gains were primarily driven by increased power output from the inboard turbines, whereas the outboard turbines were less sensitive to changes in spacing. The study also highlighted the importance of blade-passing interactions and asymmetric loading effects in closely spaced tidal turbine arrays.

Numerous experimental and numerical investigations have demonstrated that turbine spacing, array layout, ambient turbulence, and rotor geometry significantly influence wake recovery and downstream performance [5–9].

Nuernberg and Tao [6] conducted an experimental PIV study on wake characteristics in staggered tidal turbine arrays with varying turbine spacing. Four turbines with a diameter of 0.28 m were tested in a circulating water channel. The results demonstrated that lateral spacing plays a dominant role in wake recovery, whereas very close spacing leads to wake merging and reduced re-energization. These findings emphasize the importance of spacing optimization for improving downstream inflow conditions and overall array performance.

Mycek et al. [7] investigated wake interactions between two axially aligned horizontal-axis marine current turbines using scaled models in a flume tank under various inter-device spacings and ambient turbulence intensities (3% and 15%). The results showed that higher ambient turbulence significantly accelerates wake recovery and improves downstream turbine performance. At low turbulence intensity, strong wake effects persisted even at large spacings, resulting in substantial power losses for the downstream turbine.

Gotelli et al. [8] investigated wake interactions in arrays of marine hydrokinetic turbines (diameter: 0.09 m) through a combination of flume experiments and DES–BEM simulations. Using ADV measurements for two tandem turbines, they analyzed velocity deficits, turbulence characteristics, and turbine performance. Although the numerical results agreed well with the experimental data in the far wake, limitations of the DES–BEM model were identified in the near-wake region, where wake-interaction effects were not fully captured.

Ouro et al. [9] investigated the influence of inter-row spacing on the performance and loading of tidal stream turbine arrays using Large-Eddy Simulation coupled with an actuator line model (LES–ALM). Arrays consisting of two turbine rows separated by 4D and 8D were analyzed and validated against experimental data. The results showed that insufficient wake recovery at smaller spacing led to significant power loss and increased unsteady loading on downstream turbines. Increasing the spacing improved wake recovery and turbine efficiency, but it also increased fatigue loads, particularly on the back-row turbines.

Several studies highlight the influence of tip vortices and blade-induced turbulence on wake persistence and mixing, identifying them as key mechanisms that govern energy availability for downstream turbines [10–13]. Ambient turbulence intensity also plays a

critical role, with higher background turbulence accelerating wake recovery and reducing performance losses in downstream devices [14,15].

Mycek et al. [14] experimentally investigated the influence of ambient turbulence intensity on the performance and wake characteristics of a single horizontal-axis marine current turbine. Flume-tank experiments were conducted under two representative turbulence levels (3% and 15%) using detailed velocity measurements and load sensing. The results showed that, although the mean power and thrust coefficients were only weakly affected by turbulence intensity, their fluctuations increased significantly at higher turbulence levels. In contrast, wake recovery was strongly dependent on turbulence intensity, with higher turbulence promoting faster wake dissipation and enhanced mixing.

Noble et al. [15] experimentally examined the flow characteristics, performance, and structural loads of tidal turbines arranged in a closely spaced staggered array. Using large-scale model tests (diameter: 1.2 m) with ADV measurements, the authors showed that upstream turbines can accelerate the inflow to downstream turbines, resulting in increased power and thrust without inducing additional unsteady loading.

Recent research emphasizes the need for high-fidelity experimental data to validate numerical models, as computational approaches alone often struggle to accurately capture near-wake coherent structures, turbulence anisotropy, and long-range vortex evolution [16,17]. In addition, farm-scale optimization strategies—such as staggered configurations, closely spaced turbine fences, and constructive interference layouts—require reliable wake data to evaluate their practical viability and hydrodynamic impacts [12,18].

This work investigates the hydrodynamic interactions between two tidal stream turbines arranged in tandem using a mobile submersible PIV (Particle Image Velocimetry) system. By visualizing and quantifying the velocity deficit, tip vortex structures, turbulence characteristics, and wake recovery across an extended downstream distance, this work provides high-resolution experimental data that can support turbine spacing guidelines, array optimization, and future CFD validation efforts.

Despite significant progress in tidal energy research, characterizing long-range turbine–turbine interactions in tandem configurations remains a major challenge. Many previous experimental efforts have been limited by stationary measurement setups that provide insufficient downstream coverage or rely on point-measurement techniques such as Acoustic Doppler Velocimetry (ADV) [3], which lack the spatial resolution needed to resolve coherent tip vortex structures. In addition, existing PIV-based studies are often confined to the near-wake region ($x/D < 7$) due to facility constraints [6], thereby limiting the ability to capture the downstream evolution and eventual fusion of vortex filaments at larger turbine spacings. To overcome these limitations, the present study employs a mobile submerged PIV system that enables high-resolution, phase-averaged measurements over a continuous streamwise domain extending to 11.6D. This experimental framework yields a high-fidelity dataset capturing velocity deficit recovery, turbulence anisotropy, and tip vortex evolution, thereby providing critical validation data for advanced Large Eddy Simulation (LES) and other numerical approaches toward tidal array optimization.

2. Materials and Methods

2.1. Turbine Model and Circulating Water Tunnel with PIV System

Figure 1 presents a schematic diagram and photographs of the circulating water tunnel and the particle image velocimetry (PIV) system used in the experiments. A detailed description of the facility and the experimental apparatus is provided below.

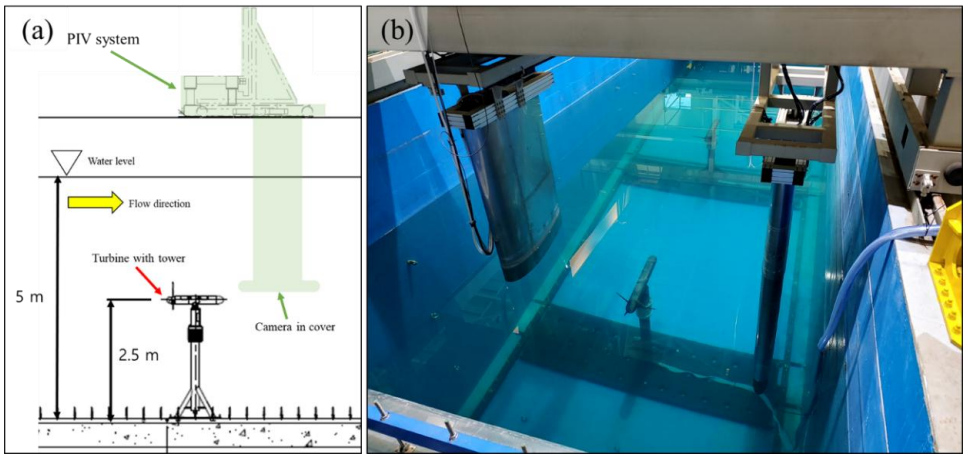

Figure 1. (**a**) Schematic diagram of the large circulating water tunnel; (**b**) the submerged PIV system configuration around the turbine.

2.1.1. Circulating Water Tunnel

The tidal stream turbine experiments were conducted in the large circulating water tunnel (CWT) located at the Marine Robotics Demonstration Center in Pohang, Gyeongsangbuk-do, South Korea. The test section of the large CWT is 20 m long, 5 m wide, and 5 m deep, and the flow velocity can be controlled up to a maximum of 1.76 m/s. The CWT consists of a horizontally aligned test section and a flow-generation section driven by an impeller. Inside the CWT, honeycomb structures and guide vanes are installed to control flow rotation and pressure, preventing flow separation and ensuring a uniform flow field in the test section.

2.1.2. Particle Image Velocimetry System

Since the large-size CWT does not have optical windows, the camera and laser must be submerged for underwater PIV (Particle image velocimetry) measurements. To reduce the complexity of deploying the camera and laser separately underwater, a PIV system was designed to allow both devices to be submerged simultaneously (see Figure 1).

The submerged portions of the camera and laser are enclosed in streamlined housings to minimize vibration induced by the flow. The camera housing and laser housing are mounted on separate traverses, enabling independent positioning along the y- and z-axes. The entire PIV system can also be moved along the rail of the CWT, allowing position adjustment in the x-axis direction.

The CCD camera has a resolution of 25 MP and a frame rate of 180 fps (Model 630098, TSI Inc., Shoreview, MN, USA). A motor-controlled zoom lens (NIKKOR 105 mm, Nikon Inc., Tokyo, Japan) is mounted on the camera, enabling easy adjustment of the field of view underwater. A 532 nm optical filter is attached to the lens to block light sources other than the laser wavelength.

The laser is a 200 mJ, 532 nm Nd:YAG laser (Quantel, Evergreen Inc., Lannion, France), and cylindrical and spherical lenses are used to generate a laser sheet with a thickness in the range of 2 mm to 5 mm.

2.1.3. Turbine Model

As shown in Figure 2a, the nacelle has a streamlined cylindrical shape with a diameter of 0.15 m and a length of 1.15 m. A removable cover is installed on the top of the nacelle, allowing easy maintenance of the equipment and various sensors housed inside (Figure 2b). The interior is equipped with a 1000 W servo motor (SGM7A-10A, Yaskawa, Kitakyushu, Japan), a Torque–RPM sensor (T21WN, HBM, Darmstadt, Germany), which has an accuracy

class of 0.2 according to the manufacturer's data sheet, and a photo sensor (PM-L25, Panasonic, Osaka, Japan) (Figure 2c). To ensure long-term operation, a highly waterproof mechanical seal was used to maintain watertightness around the rotating shaft. The watertight performance of the sensors and motor during turbine operation was verified by submerging only the turbine head, including the nacelle, in a small water tank.

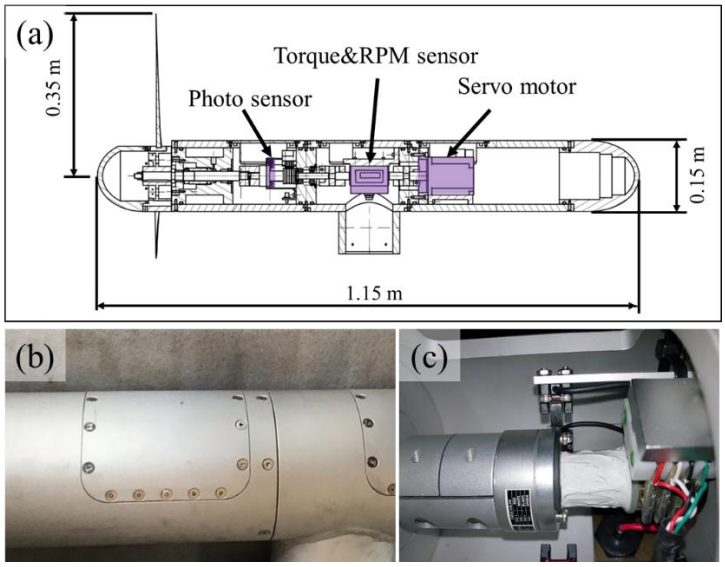

Figure 2. (**a**) Overview of the tidal turbine model, including the nacelle structure, internal components, and three-bladed rotor; (**b**) A removable cover for easy maintenance; (**c**) photo sensor for phase-averaged analysis.

The rotational speed and torque of the shaft are controlled by the servo motor installed inside the nacelle, and no gears are used for power transmission. As a result, torque and RPM can be measured without power loss due to gearing by using a torque–RPM sensor directly connected to the motor shaft. In addition, a photo sensor was used to obtain PIV measurements at identical blade positions for phase-averaged analysis. Whenever the blade passes a designated angular position, the photo sensor sends a trigger signal for the camera.

The rotor consists of three blades, each having a length of 0.35 m from the shaft center to the blade tip. The blades were manufactured using AL6061 aluminum (CIIZ, Busan, Republic of Korea), which offers excellent machinability and corrosion resistance, and they were anodized for surface protection. Based on sectional profile data along the blade span, blade element momentum theory (BEMT) and parametric analysis were performed. This process produced a blade design in which the sectional NACA profile transitions from NACA 63-824 at the root to NACA 63-813 toward the tip. Detailed information on the blades was provided in our previous study [19].

2.1.4. Tower and Base Plate

The turbine is mounted on a tower and a base plate, and is ultimately positioned at a water depth of 2.5 m. The tower has a height of 2.3 m, an outer diameter of 165 mm, and a wall thickness of 5 mm. As shown in Figure 3, to enable the placement of multiple turbines at specified locations, a base plate and rail system were designed and installed so that turbines can be arranged in increments of 0.5D.

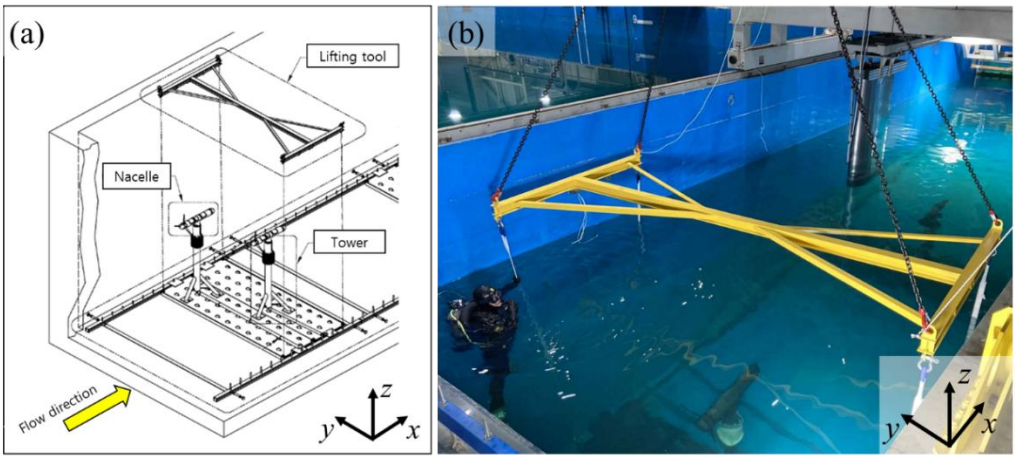

Figure 3. Tower and base-plate assembly enabling precise turbine positioning in the CWT. (**a**) Schematic diagram of turbine assembly; (**b**) turbine installation on CWT floor.

The base plate has holes through which the legs of the tower are inserted and then secured. These holes are spaced at intervals of 0.5D, allowing turbines mounted on the towers to be positioned in the y-direction in increments of 0.5D. The position of the base plate itself is determined by a pair of rails installed on CWT floor (distinct from the rails used for the PIV system on the CWT). Pins protruding from the rails at intervals of 0.5D fit into the mounting holes of the base plate, enabling the final positioning of the turbine in the x-direction in increments of 0.5D.

2.2. Measurement & Data Acquisition

2.2.1. GUI-Based Control and Data Acquisition

For the experiments, a GUI-based program was developed to integrally collect all measurement data and to operate multiple turbines simultaneously. The completed system provides the following major functionalities: It enables real-time acquisition and display of turbine rotational speed, shaft torque, photo-sensor signals, three-axis force, three-axis moment, and other experimental data according to predefined storage formats (Figure 4a). In addition, the system allows independent control of each turbine's servo motor for blade rotation and torque input (Figure 4b).

2.2.2. Setup of Data Acquisition Devices

Using the previously described turbine setup, torque and rotational speed were measured with a Torque–RPM sensor (T21WN, HBM). Data acquisition was performed using a QuantumX MX840A DAQ (data acquisition) system manufactured by HBM (Figure 5a). The analog outputs of the Torque–RPM sensor were digitized through the input channels of the DAQ. Because electrical noise generated by the servo driver (SGD7S-120A00A, Yaskawa) can interfere with the sensor signals, an EMC filter (AB3CZ-4015, Oky, Anyang, Republic of Korea) was installed at the driver output to mitigate this issue (Figure 5c).

The data collected from both turbines were transmitted to a PC via an Ethernet interface, and real-time monitoring and recording were carried out using the catman® AP software (version 5.0.1.39, HBM). The PC used for data processing was equipped with an Intel Core i7-6700HQ CPU and 16 GB of memory (Figure 5b).

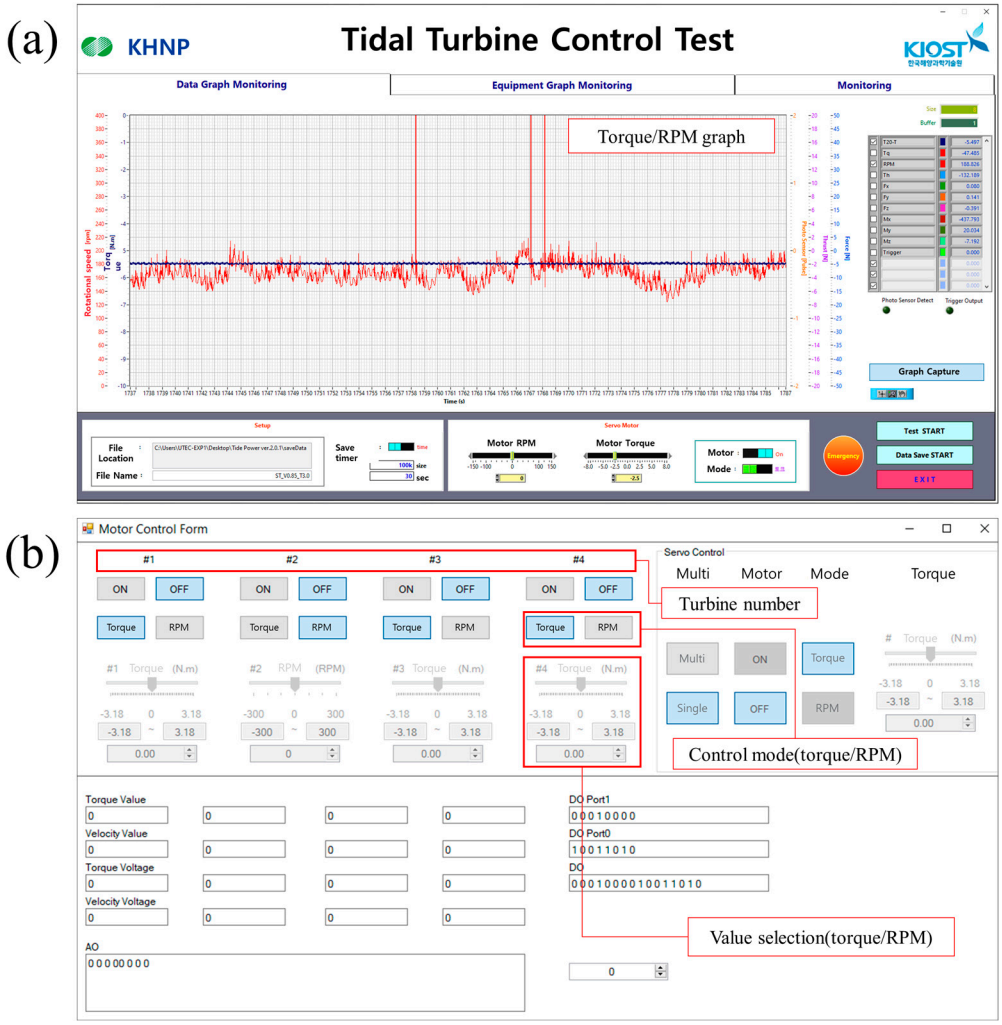

Figure 4. GUI-based (**a**) data acquisition system and (**b**) control system used for real-time monitoring of turbine torque, rotational speed, and multi-axis load measurements.

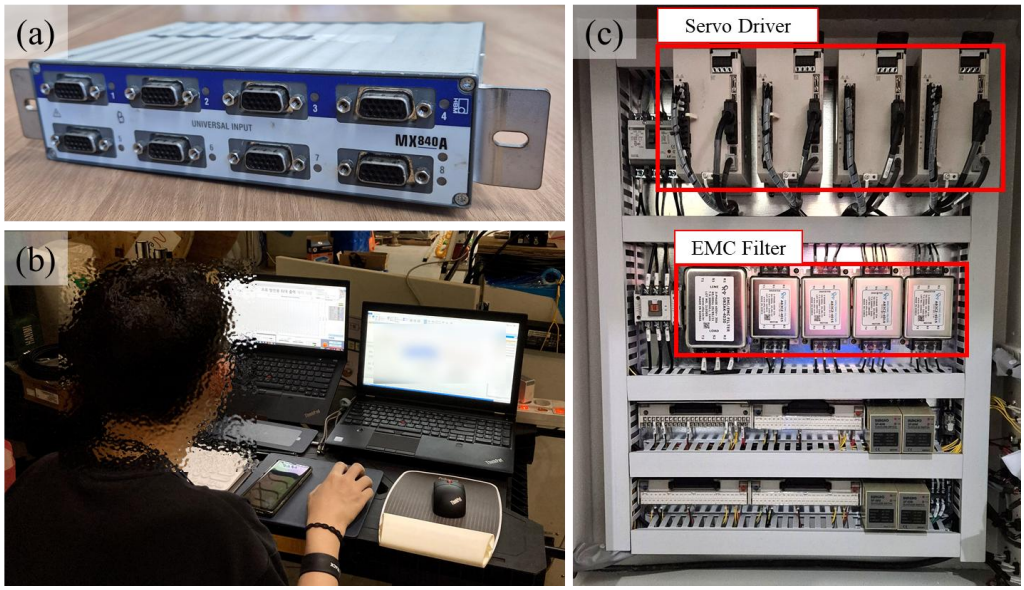

Figure 5. Data acquisition setup using the HBM QuantumX system including noise-mitigation components (EMC Filter). (**a**) DAQ of HBM QuantumX; (**b**) data collecting with HBM QuantumX system; (**c**) servo driver and EMC filter.

2.3. Experiment Configuration

2.3.1. Installation of Turbine Models

Both turbines are positioned at a depth of 2.5 m within the 5 m deep water channel and are located 2.5 m away from the sidewalls of the 5 m wide tank, placing them at the center of the cross-section. Figure 6 presents the arrangement of two tidal turbines in tandem. Turbine 1 is positioned 6D (4.2 m) downstream from the CWT inlet, while Turbine 2 is located 10D (7 m) downstream from Turbine 1.

A spacing of 10D (7 m) was secured to analyze the interaction effects between Turbine 1 and Turbine 2, while the position of Turbine 1 was limited to 4.2 m from the inlet due to physical constraints imposed by the equipment.

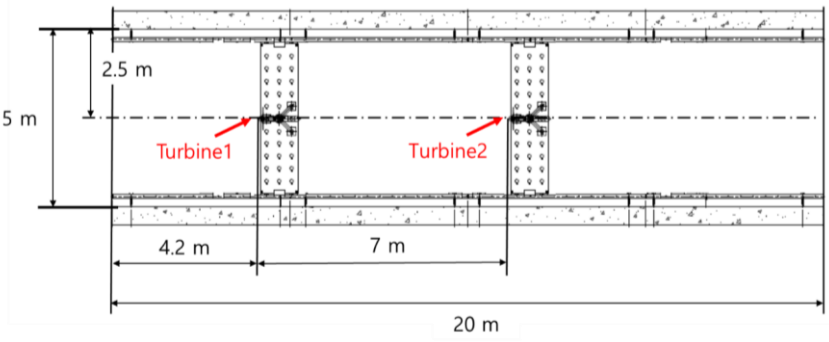

Figure 6. Experimental arrangement of two tidal turbines in tandem within the CWT showing the longitudinal spacing (10D).

2.3.2. Power Take-Off Test

The performance of the upstream turbine and the performance of the downstream turbine subjected to the wake of the upstream turbine were measured. To evaluate turbine performance through power take-off (PTO) test, the power coefficient (C_P) is calculated from the tip–speed ratio (TSR) as follows.

$$\mathrm{TSR} = \frac{r\Omega}{U}, \tag{1}$$

where r is radius of the turbine, Ω is the angular velocity (rad/s), and U is the incoming velocity.

Powe coefficient (C_P) is defined by following equation.

$$C_P = \frac{\Omega T}{0.5\rho U^3 \pi r^2}, \tag{2}$$

where T is the torque and ρ is the density of water (at 18 °C, the density of water is 998.60 kg/m^3).

The experimental flow velocity was 0.77 m/s, and an additional load was applied to the turbine shaft by imposing a counteracting torque—opposite to the rotational direction—using a servo motor while the turbine was rotating under the incoming flow. Although the torque applied by the servo motor was identical for Turbine 1 and Turbine 2, the total shaft torque could differ because the inflow conditions for the two turbines were not the same. This method allowed control of the turbines' TSRs, enabling comparison of the resulting variations in efficiency.

2.3.3. PIV Imaging Configuration

PIV measurements of the wake behind Turbine 1 were conducted under the previously described arrangement of Turbine 1 and Turbine 2. As shown in Figure 7, the horizontal distance between the camera and the laser sheet was 1.6 m, providing a field of view (FoV) of 0.35 m × 0.35 m with a spatial resolution of 68.6 × 68.6 µm/pixel at this position.

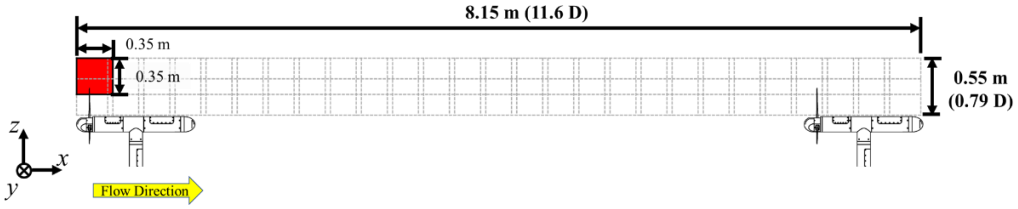

Figure 7. PIV imaging configuration illustrating camera–laser alignment, field of view, and measurement domain.

The camera of the PIV system was traversed 0.3 m in the x-direction and 0.2 m in the z-direction, resulting in FoV overlaps of 0.05 m in the x-direction and 0.15 m in the z-direction between adjacent measurement regions. A total of 27 sections in the x-direction and 2 sections in the z-direction were acquired. Consequently, the entire measurement domain corresponds to 8.15 m (11.6D) in the x-direction and 0.55 m (0.79D) in the z-direction. Within this domain, the flow from the leading edge of Turbine 1 to the trailing end of Turbine 2 can be observed.

The flow velocity during the PIV measurements was set to 0.77 m/s, consistent with the turbine performance tests. To ensure stable long-duration operation, the TSRs of Turbine 1 and Turbine 2 were maintained at approximately 7.6 and 6.32, respectively, resulting in power coefficients of approximately 0.45 and 0.35. Polyamide tracer particles (1101-1000, Intech Systems, Ahmedabad, India) with a diameter of 100 µm and a density of 1.1 g/cm^3 were used. To verify the particle tracking capability, the Stokes number (St) was estimated. For an experimental flow velocity of 0.77 m/s and a characteristic blade length scale, the Stokes number was found to satisfy St $\ll$ 1, indicating that the seeding particles closely follow the water flow with minimal slip. In addition, the seeding density was adjusted to ensure at least 10 particle images per 128 $\times$ 128 pixel interrogation window (corresponding to approximately 8.78 mm $\times$ 8.78 mm), providing sufficient particle image density for reliable cross-correlation and robust PIV measurements in high-shear regions such as the blade tips.

The laser sheet was illuminated above the turbine, and the time interval between laser pulses for each image pair was 3000 µs. A photo sensor detected the moment when a blade of Turbine 1 passed the 12 o'clock position, and 256 image pairs were captured for each measurement section before conducting phase averaging. The 1% fluctuation threshold for the moving average is a widely accepted criterion for assessing statistical convergence in experimental fluid mechanics [20]. In this study, 256 image pairs were acquired based on pre-test evaluations and established methodologies for tidal turbine wake measurements in large-scale water tunnels. As demonstrated in our previous work [19], this sample size is sufficient to resolve coherent tip vortex structures and stable velocity deficits in the wake region up to 10D downstream.

PIV images were acquired and processed using Insight 4G (version 11.1.0.7, TSI Inc.). The Recursive Nyquist Grid engine was employed to generate interrogation windows with 50% overlap, and particle spots were filtered using a Gaussian mask. The initial interrogation window size was 256 $\times$ 256 pixels, and the final window size was reduced to 128 $\times$ 128 pixels. Correlation maps were computed using a Fast Fourier Transform (FFT) correlator. The uncertainty of the PIV measurements was quantified using the peak-to-noise peak ratio (PPR)-based uncertainty estimation implemented in the Insight4G PIV analysis software. This method evaluates the reliability of the correlation peaks associated with the displacement vectors. The resulting velocity uncertainty was estimated to be approximately 3.2% at the 95% confidence level.

3. Results and Discussion

3.1. Comparison via Power Take-Off Test

The experimental C_P values of the turbine model are shown in Figure 8. The C_P values of Turbine 1 are shifted toward higher TSR (tip speed ratio) regime but remain in good agreement with the BEMT predictions for a blade using NACA63-8xx profiles reported in a previous study [21], which employed a blade geometry similar to that used in the present study. For Turbine 1, C_P was measured over a TSR range of 7.3–10.1. For Turbine 2, C_P was measured over a TSR range of 5.9–8.9, and both the operational TSR range and C_P values were generally lower than those of Turbine 1, with the maximum C_P reduced by approximately 9%. Across the TSR ranges examined, the Reynolds numbers based on relative velocity are greater than 10^5 under the present experimental conditions.

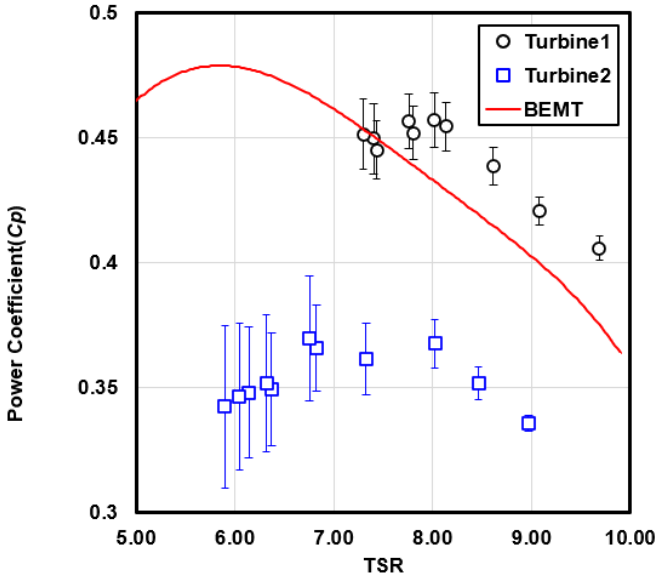

Figure 8. Power coefficient (C_P) values of Turbine 1 and Turbine 2 versus TSR.

Because counter-loading was applied by the servo motor during the experiments, reverse rotation occurred at low TSRs, making further efficiency measurements impossible in that range. In particular, for the downstream turbine, the inflow altered by the upstream turbine led to larger error bars and a more unstable efficiency distribution under low-TSR conditions.

Additionally, due to the counter-loading from motor control and the mechanical seal used for extended underwater operation, the maximum C_P of the downstream turbine was lower than the design value predicted by BEMT, yielding a maximum C_P of 37%, which occurred at TSR 6.75.

3.2. Wake Characteristics

The flow conditions within the PIV measurement domain were verified. Using the PIV data, the velocity values in the overlapping regions were calculated through arithmetic averaging, after which the velocity deficit, turbulence intensity (TI), turbulent kinetic energy (TKE), and normalized vorticity were derived. Each result is presented in Figure 9 in the form of contour plots. Details of each indicator used to characterize the wake are provided in the following sections.

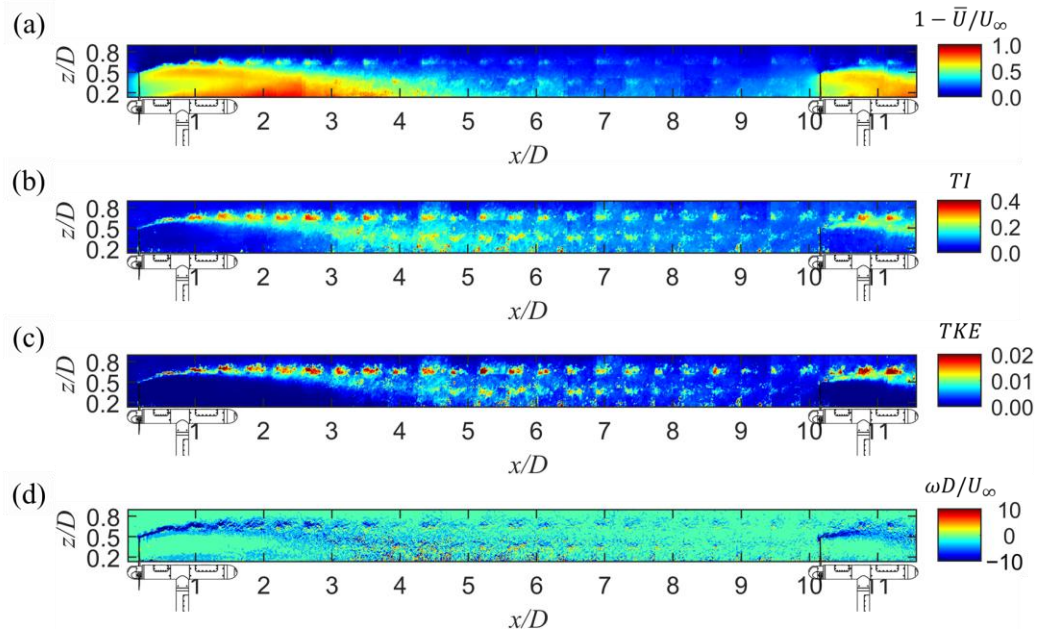

Figure 9. Overview of the wake-field variables obtained from PIV, including (**a**) velocity deficit; (**b**) turbulence intensity; (**c**) turbulent kinetic energy; (**d**) normalized vorticity.

3.2.1. Velocity Distribution

The velocity distributions downstream of Turbine 1 and Turbine 2 are shown in Figure 10 in the form of velocity deficit, defined by the equation below. The velocity deficit represents the reduction in flow velocity relative to the free-stream velocity and is obtained by normalizing the difference between the free-stream velocity and the phase-averaged wake velocity, $(U_\infty - \overline{U})$, by the free-stream velocity (U_∞).

$$\text{Velocity deficit} = \frac{U_\infty - \overline{U}}{U_\infty} = 1 - \frac{\overline{U}}{U_\infty}. \quad (3)$$

The flow velocity of the downstream turbine decreased significantly compared to the free-stream velocity. At downstream locations of x/D = 2, 5, and 10, the wake core widths were measured as 0.54D, 0.34D, and 0.36D, respectively, while the corresponding maximum velocity deficits were 0.89, 0.48, and 0.40. Overall, the velocity deficit decreased with increasing downstream distance, and the wake core narrowed substantially from x/D = 2 to 5, followed by a slight increase at x/D = 10. For Turbine 1, the wake gradually expanded downstream from the blade region in the streamwise direction. The velocity deficit began even upstream of the blade plane, and its dominant influence originated from both the blade tip and root. The velocity deficit originating from the blade tip expanded immediately in the +z direction. As the flow progressed in the x-direction, the deficit intensified, and the deficit generated at the blade tip increased up to x/D = 1 before it began merging with the deficit generated at the blade root as shown in Figure 10b.

The velocity deficit originating from the blade root expanded in the +z direction while following the contour of the nacelle body, increasing in magnitude until approximately x/D = 2.5. The influence of the velocity deficit persisted up to around x/D = 6.5, after which a recovery trend was observed.

Another notable feature is the presence of the tip vortices generated at the blade tips. These vortices are produced by the vortex filaments, and in this study, their structure could be clearly identified through phase-averaged PIV measurements. After being shed from the blade tip, the tip vortices traveled slightly in the +z direction and appeared along the

x-axis at nearly uniform spacing (approximately 4.5D) at z/D = 0.67. Remarkably, they remained visible up to the location of Turbine 2, which was positioned 10D downstream.

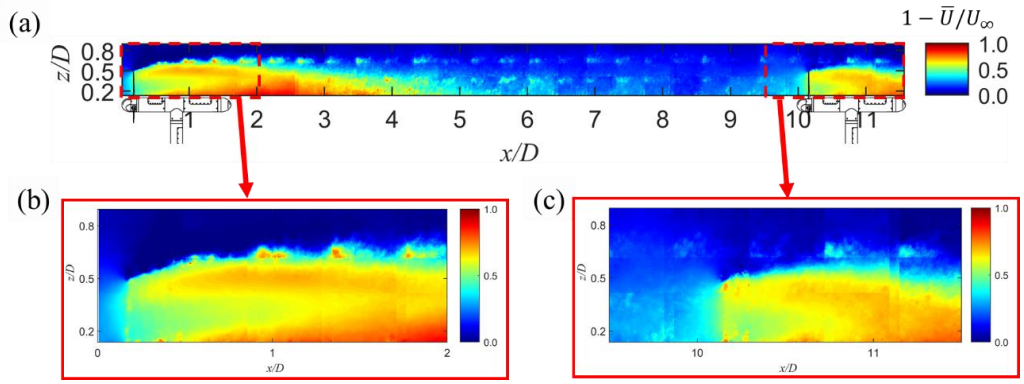

Figure 10. Distribution of velocity deficit within the turbine wake. (**a**) velocity distribution over the entire measurement domain; (**b**) Enlarged view of the near-wake region downstream of Turbine 1; (**c**) Enlarged view of the near-wake region downstream of Turbine 2.

Due to physical constraints and potential interference between the PIV system and other experimental equipment mounted on the rail, the PIV system could not be moved to the downstream end of the water tunnel. As a result, the wake of Turbine 2 was imaged only up to the nacelle location. While the velocity deficit had largely recovered at 10D downstream of Turbine 1, the aforementioned tip vortices were still present. The velocity deficit originating from the blade tips of Turbine 2 grew and merged more rapidly than in the case of Turbine 1; however, it did not appear to expand as extensively in the +z direction.

3.2.2. Turbulence Intensity

Turbulence intensity is defined as the ratio of the standard deviation of the velocity to the mean velocity at a given location, and is expressed by the following equation.

$$\mathrm{TI} = \frac{\sqrt{\overline{(u')^2} + \overline{(w')^2}}}{\overline{U}}, \tag{4}$$

where u' is the standard deviation of the flow velocity (u) in the x-direction and w' is the standard deviation of the flow velocity (w) in the z-direction. In the turbulence intensity distribution within the wake (Figure 11), the structure of the tip vortices was more visibly identifiable than in the velocity deficit plots. For Turbine 1, the primary region of elevated turbulence intensity originated at the blade tips, and the formation of the tip vortex structure became evident at approximately x/D = 0.5. As also noted in the velocity deficit results, the tip vortices appeared at regular intervals. Independent of the high turbulence intensity occurring at the tip vortices, the turbulence intensity increased from the wake boundary toward the wake core. The ambient turbulence intensity of the free stream was measured to be 0.038, whereas the mean turbulence intensity in the wake of the same turbine was 0.17 at a free-stream velocity of 1 m/s in the same facility [19]. This low ambient turbulence level ensures that the wake recovery and vortex persistence observed in this study are primarily governed by turbine-induced hydrodynamic interactions rather than background flow fluctuations. In the region of x/D = 3–5, the turbulence intensity field became complex, making it difficult to distinguish any specific structures. Beginning at x/D = 3.4, the tip vortices were observed to organize into two nearly horizontal rows located at z/D = 0.4 and z/D = 0.7. The breakdown of the tip vortex observed around x/D ≈ 3 is likely the result of a combination of physical mechanisms rather than a single instability. As the wake develops downstream, the shear layer between the low-momentum wake core and

the surrounding higher-speed flow grows, enhancing turbulent mixing and leading to vortex-core stretching and attenuation.

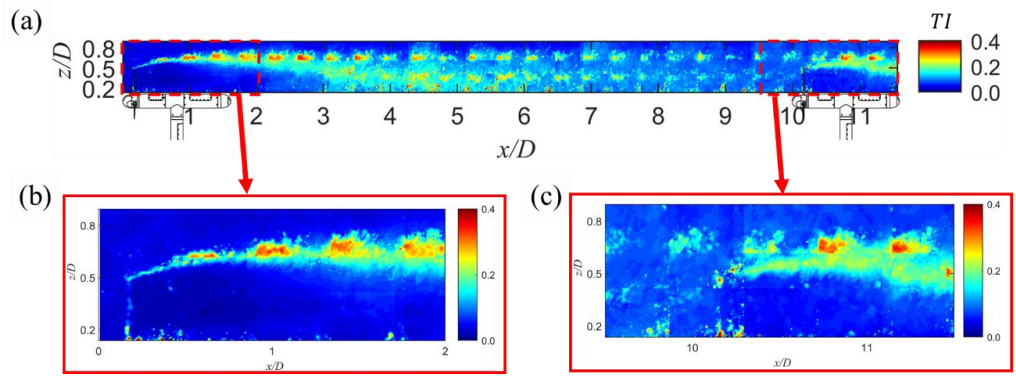

Figure 11. Turbulence intensity (TI) distribution within the turbine wake. (**a**) TI distribution over the entire measurement domain; (**b**) Enlarged view of the near-wake region downstream of Turbine 1; (**c**) Enlarged view of the near-wake region downstream of Turbine 2.

In addition, previous studies [22,23] have reported that adjacent helical tip vortices may undergo pairing instabilities driven by mutual induction, resulting in the formation of larger vortex structures and subsequent wake breakdown. The present observations of vortex-core expansion and reduced vorticity magnitude are consistent with this behavior. However, due to the limitations of the 2D-PIV measurements, the three-dimensional features of vortex pairing cannot be resolved directly. Future studies employing three-dimensional measurement techniques or high-fidelity numerical simulations are therefore required to elucidate the detailed breakdown mechanism.

In the vicinity of Turbine 2, the merging of tip vortices could be clearly identified. The tip vortices shed from Turbine 1 persisted up to approximately x/D = 10.4, after which they merged with the vortices generated by Turbine 2 around x/D = 10.8. The merged vortex structure was positioned further in the +z direction compared to the initial vortex shed from Turbine 1 at x/D = 0.5, and it exhibited a larger size and higher turbulence intensity. The turbulence intensity at z/D = 0.4 remained detectable up to the turbine blades of Turbine 2. Downstream of the blade passage, however, the vortex structures became indistinct and no consistent pattern was observed.

3.2.3. Turbulent Kinetic Energy

Turbulent kinetic energy (TKE) is defined as half the sum of the variances of the velocity components, as expressed in the following equation.

$$\mathrm{TKE} = \frac{1}{2}\left(\overline{(u')^2} + \overline{(w')^2}\right), \tag{5}$$

While turbulence intensity represents the relative proportion of turbulence compared to the mean velocity, turbulent kinetic energy directly reflects the amount of turbulent energy present in the wake. Unlike the complex TI distribution observed for x/D > 3, the TKE distribution clearly reveals the regions of elevated turbulent energy, as shown in Figure 12. TI and TKE were used to define the decay region, transition region, and far-wake region of a single turbine in a previous study [19], and they could similarly be used to characterize these regions for a turbine influenced by the wake of an upstream device.

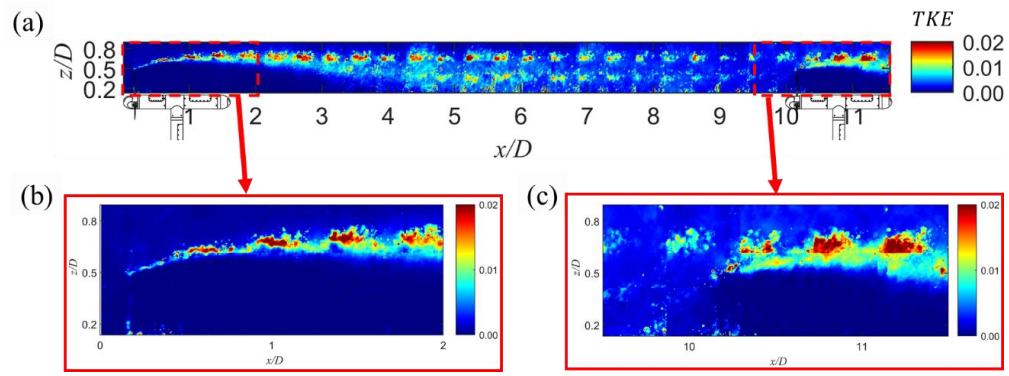

Figure 12. Turbulent kinetic energy (TKE) distribution within the turbine wake. (**a**) TKE distribution over the entire measurement domain; (**b**) Enlarged view of the near-wake region downstream of Turbine 1; (**c**) Enlarged view of the near-wake region downstream of Turbine 2.

3.2.4. Vorticity

The contours of normalized vorticity ($\omega D/U_\infty$), where ω is vorticity, provide further insight into the coherent structures governing the wake dynamics of the tandem turbine configuration (Figure 13). Distinct regions of strong negative-signed vorticity were observed at the blade tips of Turbine 1, confirming the formation of well-defined tip vortices immediately downstream of the rotor plane. These vortices maintained their identity over a substantial downstream distance, despite gradual dissipation beginning around x/D ≈ 2. The persistence of these coherent structures aligns with the behavior noted in the turbulence intensity and velocity deficit fields, where periodic vortex patterns were also visible.

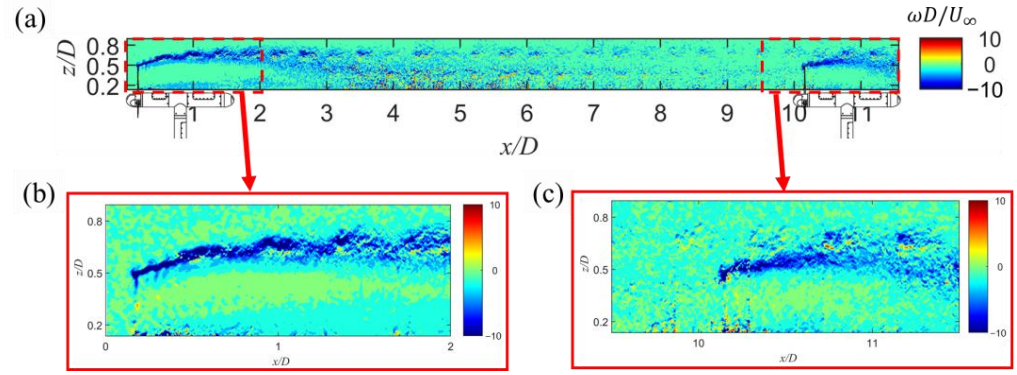

Figure 13. Normalized vorticity distribution within the turbine wake. (**a**) vorticity distribution over the entire measurement domain; (**b**) Enlarged view of the near-wake region downstream of Turbine 1; (**c**) Enlarged view of the near-wake region downstream of Turbine 2.

A notable feature revealed by the vorticity field is the splitting and deformation of the tip vortex cores as they move downstream. Around x/D ≈ 3, the initially compact vortices began to elongate and fragment into multiple smaller-scale eddies. This transition indicates the onset of vortex breakdown driven by increased turbulence levels and wake shear interactions. Beyond this region, the wake loses its coherent large-scale structure, becoming dominated by irregular eddy distributions. This behavior corresponds with the rapid rise in turbulent kinetic energy, suggesting that vortex-induced mixing plays a major role in wake recovery.

In addition, the vorticity contours highlight how the wake of Turbine 1 influences the flow approaching Turbine 2. Although the velocity deficit had largely diminished by 10D downstream, remnants of the tip vortices remained detectable and continued to move toward the downstream turbine. These distorted vortical structures likely contributed to the modified inflow conditions of Turbine 2, promoting early vortex merging and increased

turbulence near its blade passage. Such interactions help explain the reduced performance observed in the downstream turbine's PTO measurements.

Overview of peak values of velocity deficit, and peak values of tip vortices, including turbulent kinetic energy, and normalized vorticity are presented in Figure 14, where the three tip vortex structures generated by Turbine 1 could be compared with those generated by Turbine 2. For Turbine 1, the downstream locations of the three vortices were 0.64D, 0.98D, and 1.36D, with corresponding peak vorticity values of 19.26, 16.16, and 14.14, respectively. For Turbine 2, the vortices were observed at 10.39D, 10.71D, and 11.17D, with peak vorticity values of 10.97, 8.37, and 8.88, respectively. The vortex diameters of Turbine 1 were 0.088D, 0.113D, and 0.175D, whereas those of Turbine 2 were 0.207D, 0.275D, and 0.313D, respectively. Compared with Turbine 1, the tip vortices of Turbine 2 were shifted upstream. Although the peak TKE values showed no significant variation, the vortex diameters increased substantially.

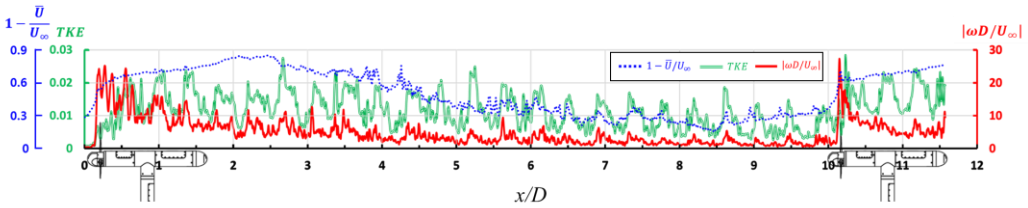

Figure 14. Overview of peak values of velocity deficit, and peak values of tip vortices, including turbulent kinetic energy, and normalized vorticity.

4. Conclusions

This study experimentally investigated the hydrodynamic interactions between two horizontal-axis tidal turbines arranged in tandem. The incoming flow was dominated by the streamwise velocity component, as no external disturbances were imposed; thus, the inflow conditions do not fully represent the complexity of real tidal environments. The integrated submergible turbine–PIV setup in a large circulating water tunnel enabled high-resolution measurements of wake structures, velocity deficits, turbulence characteristics, and vortex evolution over an extended downstream region encompassing both turbines.

Performance measurements revealed relative performance trends between the two turbines, indicating that the downstream turbine experienced reduced efficiency, with a maximum power coefficient approximately 9% lower than that of the upstream turbine. This reduction was attributed to the altered inflow conditions imposed by the upstream turbine, including decreased local velocity and elevated turbulence levels.

Phase-averaged PIV measurements revealed detailed wake dynamics behind the upstream turbine. Strong velocity deficits originated from both the blade tip and root regions, exhibiting gradual recovery up to approximately 6.5D downstream. Tip vortices shed from the upstream turbine persisted remarkably far downstream, maintaining coherent spacing and remaining detectable up to the location of the downstream turbine at 10D. These vortices merged with those generated by the downstream turbine, forming enlarged, more energetic vortex structures that influenced the near-wake characteristics of Turbine 2. To mitigate the impact of tip vortices shed by upstream turbines, a streamwise spacing of more than 10D or the adoption of a staggered array configuration should be considered. Turbulence intensity and turbulent kinetic energy distributions further highlighted the presence of complex mixing, vortex merging, and elevated turbulent activity in the turbine-to-turbine interaction zone.

Overall, the results provide experimental evidence of long-range vortex persistence and significant wake interference effects in tandem turbine configurations. The findings un-

derscore the importance of accurate wake characterization for optimizing turbine spacing, array layouts, and control strategies in tidal energy farms. The high-resolution PIV dataset presented in this study would offer valuable reference data for validating numerical models and improving predictive capabilities for multi-turbine systems. Future studies will extend the present work by examining a wider range of turbine spacings, inflow turbulence levels, and more realistic environmental conditions.

Author Contributions: Resources, H.L.; supervision, J.K.; writing—original draft preparation, S.J.; writing—review and editing, J.H.K.; analysis, I.S.J.; technical support—installation, H.K. and C.H.S.; and measurement, S.M.M. All authors have read and agreed to the published version of the manuscript.

Funding: This work was supported by Korea Hydro & Nuclear Power Co., Ltd. (grant code: A18LP08) and was supported by the Regional Innovation System & Education (RISE) program through the Jeju RISE center, funded by the Ministry of Education (MOE) and the Jeju Special Self-Governing Province, Republic of Korea (2025-RISE-17-001).

Data Availability Statement: Data are contained within the article.

Conflicts of Interest: Author Heebum Lee was employed by Korea Hydro & Nuclear Power Co., Ltd. The remaining authors declare that the research was conducted in the absence of any commercial or financial relationships that could be construed as a potential conflict of interest.

References

1. Chamorro, L.; Hill, C.; Morton, S.; Ellis, C.; Arndt, R.; Sotiropoulos, F. On the interaction between a turbulent open channel flow and an axial-flow turbine. *J. Fluid Mech.* **2013**, *716*, 658–670. [CrossRef]
2. Churchfield, M.J.; Li, Y.; Moriarty, P.J. A large-eddy simulation study of wake propagation and power production in an array of tidal-current turbines. *Philos. Trans. R. Soc. A Math. Phys. Eng. Sci.* **2013**, *371*, 20120421. [CrossRef]
3. Kang, S.; Kim, Y.; Lee, J.; Khosronejad, A.; Yang, X. Wake interactions of two horizontal axis tidal turbines in tandem. *Ocean Eng.* **2022**, *254*, 111331. [CrossRef]
4. McNaughton, J.; Ettema, S.; De Arcos, F.Z.; Vogel, C.; Willden, R. An experimental investigation of the influence of inter-turbine spacing on the loads and performance of a co-planar tidal turbine fence. *J. Fluids Struct.* **2023**, *118*, 103844. [CrossRef]
5. Nuernberg, M.; Tao, L. Experimental Study of Flow Field Characteristics in Tidal Stream Turbine Arrays. In Proceedings of the International Conference on Offshore Mechanics and Arctic Engineering, Busan, Republic of Korea, 19–24 June 2016; American Society of Mechanical Engineers: New York, NY, USA, 2016; p. V006T09A004.
6. Nuernberg, M.; Tao, L. Experimental study of wake characteristics in tidal turbine arrays. *Renew. Energy* **2018**, *127*, 168–181. [CrossRef]
7. Mycek, P.; Gaurier, B.; Germain, G.; Pinon, G.; Rivoalen, E. Experimental study of the turbulence intensity effects on marine current turbines behaviour. Part II: Two interacting turbines. *Renew. Energy* **2014**, *68*, 876–892. [CrossRef]
8. Gotelli, C.; Musa, M.; Guala, M.; Escauriaza, C. Experimental and numerical investigation of wake interactions of marine hydrokinetic turbines. *Energies* **2019**, *12*, 3188. [CrossRef]
9. Ouro, P.; Ramírez, L.; Harrold, M. Analysis of array spacing on tidal stream turbine farm performance using Large-Eddy Simulation. *J. Fluids Struct.* **2019**, *91*, 102732. [CrossRef]
10. Chen, Y.; Lin, B.; Lin, J.; Wang, S. Experimental study of wake structure behind a horizontal axis tidal stream turbine. *Appl. Energy* **2017**, *196*, 82–96. [CrossRef]
11. Di Felice, F.; Capone, A.; Romano, G.P.; Pereira, F.A. Experimental study of the turbulent flow in the wake of a horizontal axis tidal current turbine. *Renew. Energy* **2023**, *212*, 17–34. [CrossRef]
12. Ouro, P.; Nishino, T. Performance and wake characteristics of tidal turbines in an infinitely large array. *J. Fluid Mech.* **2021**, *925*, A30. [CrossRef]
13. Tang, H.; Lam, K.-M.; Shum, K.-M.; Li, Y. Wake effect of a horizontal axis wind turbine on the performance of a downstream turbine. *Energies* **2019**, *12*, 2395. [CrossRef]
14. Mycek, P.; Gaurier, B.; Germain, G.; Pinon, G.; Rivoalen, E. Experimental study of the turbulence intensity effects on marine current turbines behaviour. Part I: One single turbine. *Renew. Energy* **2014**, *66*, 729–746. [CrossRef]
15. Noble, D.R.; Draycott, S.; Nambiar, A.; Sellar, B.G.; Steynor, J.; Kiprakis, A. Experimental assessment of flow, performance, and loads for tidal turbines in a closely-spaced array. *Energies* **2020**, *13*, 1977. [CrossRef]

16. Salunkhe, S.; El Fajri, O.; Bhushan, S.; Thompson, D.; O'Doherty, D.; O'Doherty, T.; Mason-Jones, A. Validation of tidal stream turbine wake predictions and analysis of wake recovery mechanism. *J. Mar. Sci. Eng.* **2019**, *7*, 362. [CrossRef]
17. Zhang, Y.; Fernandez-Rodriguez, E.; Zheng, J.; Zheng, Y.; Zhang, J.; Gu, H.; Zang, W.; Lin, X. A review on numerical development of tidal stream turbine performance and wake prediction. *IEEE Access* **2020**, *8*, 79325–79337. [CrossRef]
18. Jordan, C.; Dundovic, D.; Fragkou, A.K.; Deskos, G.; Coles, D.S.; Piggott, M.D.; Angeloudis, A. Combining shallow-water and analytical wake models for tidal array micro-siting. *J. Ocean. Eng. Mar. Energy* **2022**, *8*, 193–215.
19. Jung, S.; Lee, H.; Jeong, D.; Kim, J.; Ko, J.H. Study on the Wake Characterization of a Horizontal-Axis Tidal Stream Turbine Utilizing a PIV System in a Large Circulating Water Tunnel. *Energies* **2025**, *18*, 1870. [CrossRef]
20. Adrian, R.J.; Westerweel, J. *Particle Image Velocimetry*; Cambridge University Press: Cambridge, UK, 2011.
21. Batten, W.M.J.; Bahaj, A.S.; Molland, A.F.; Chaplin, J.R. The prediction of the hydrodynamic performance of marine current turbines. *Renew. Energy* **2008**, *33*, 1085–1096. [CrossRef]
22. Quaranta, H.U.; Brynjell-Rahkola, M.; Leweke, T.; Henningson, D.S. Local and global pairing instabilities of two interlaced helical vortices. *J. Fluid Mech.* **2019**, *863*, 927–955. [CrossRef]
23. Marten, D.; Paschereit, C.O.; Huang, X.; Meinke, M.; Schroeder, W.; Mueller, J.; Oberleithner, K. Predicting wind turbine wake breakdown using a free vortex wake code. *AIAA J.* **2020**, *58*, 4672–4685. [CrossRef]